Check for updates

Advanced Electronic Materials

ADVANCED ELECTRONIC MATERIALS Open Access

www.advelectronicmat.de

RESEARCH ARTICLE OPEN ACCESS

Metal Cation Chemistry and Amorphous Structure Governing Hydrogen Tolerance in Oxide Semiconductor Channels for 3D DRAM

Seong-Hwan Ryu[1] | Sun Myung Lee[2] | Kwang-Hee Lee[3] | Jee-Eun Yang[3] | Sangwook Kim[3] | Jin-Seong Park[1,2]

[1]Division of Materials Science and Engineering, Hanyang University, Seoul, Republic of Korea | [2]Department of Semiconductor Engineering, Hanyang University, Seoul, Republic of Korea | [3]Future Tech Platform, Samsung Advanced Institute of Technology, Samsung Electronics, Suwon, Republic of Korea

Correspondence: Jin-Seong Park (jsparklime@hanyang.ac.kr)

Received: 26 April 2026 | **Revised:** 6 August 2026 | **Accepted:** 3 September 2026

Keywords: atomic layer deposition (ALD) | dynamic random-access memory (DRAM) application | hydrogen tolerance | indium tin gallium oxide (ITGO) | oxide semiconductors

ABSTRACT

This study analyzed hydrogen tolerance in oxide semiconductors subjected to high-temperature H_2 annealing (400–600°C), considering different metal species and crystallinities. First, various amorphous ternary oxides with fixed 1:1 at.% cation ratios were evaluated to isolate elemental effects; in the order Zn, Ga, In, and Sn, thickness retention improved while variations in carrier concentration (n_e) and Hall mobility (μ_{Hall}) decreased. Next, ternary oxide films with identical compositions were tuned by pre-annealing temperature to obtain crystalline or amorphous phase; the crystalline films exhibited enhanced etching and larger changes in n_e and μ_{Hall} that are consistent with grain boundary effects. Guided by these observations, amorphous In–Sn–Ga–O (ITGO) was benchmarked against conventional In–Ga–Zn–O (IGZO). The ITGO film maintained a thickness change below 1% with limited Hall variation after H_2 annealing at 600°C. By contrast, the IGZO film exhibited an abrupt increase in n_e exceeding three orders of magnitude after H_2 annealing at 500°C, then exhibited etching at 600°C. The application of ITGO in a field-effect transistor preserved switching characteristics after H_2 annealing up to 600°C, indicating its potential as a channel material for dynamic random-access memory compatible with high-temperature hydrogen thermal budgets.

1 | Introduction

Recent advances in artificial intelligence have accelerated the demand for large-scale data storage, driving the continuous downscaling and integration of dynamic random-access memory (DRAM) devices [1, 2]. However, conventional Si-based semiconductors suffer from an intrinsically narrow bandgap that inevitably increases the leakage current as the channel length decreases. Consequently, an excessive refresh power is required, presenting a fundamental limitation for further scaling [3]. Researchers have attempted to overcome the leakage current limitations of Si semiconductors by developing next-generation oxide semiconductor (OS) channel materials for DRAM transistors. These materials simultaneously exhibit an extremely low off-current below 10^{-18} A/μm and relatively high electron mobility of approximately 50 cm^2/Vs even in the amorphous phase [4–7]. Furthermore, the deposition-friendly nature of OSs facilitates the efficient fabrication of vertical channel devices and stacked architectures [8]. Consequently, OS transistors fabricated using atomic layer deposition (ALD), which provides step

Seong-Hwan Ryu and Sun Myung Lee contributed equally to this work.

This is an open access article under the terms of the Creative Commons Attribution License, which permits use, distribution and reproduction in any medium, provided the original work is properly cited.
© 2026 The Author(s). *Advanced Electronic Materials* published by Wiley-VCH GmbH

coverage superior to that of physical vapor deposition, have been actively explored for use in highly integrated three-dimensional (3D) memory applications [9].

Notably, OSs inherently contain various defects that act as subgap states, among which hydrogen-related defects play a particularly critical role [10]. In contrast to Si semiconductors, in which hydrogen typically passivates defects, the behavior of hydrogen in OSs depends on the surrounding metal cations, leading to variations in defect formation energy and electronic state levels that determine the shallow donor or acceptor characteristics [11, 12]. Hydrogen-induced defects cause threshold voltage (V_{TH}) shifts, hump phenomena, and mobility degradations that significantly alter the electrical characteristics of semiconductor devices [13, 14]. Furthermore, under high-temperature conditions, hydrogen can induce physical degradation such as metal clustering, metal precipitation within the film, and etching via gaseous hydride formation [15, 16]. These issues become particularly critical during DRAM fabrication, when high-temperature processes performed after transistor formation facilitate the ready diffusion of hydrogen from adjacent hydrogen-rich layers into the channel region [17]. Therefore, suppressing hydrogen diffusion alone is insufficient, and hydrogen-induced physical and electrical degradation of OSs remains a key constraint limiting their application in DRAM. Addressing this constraint necessitates further investigation of hydrogen-resistant materials and the factors that determine hydrogen stability.

The hydrogen resistance in an OS is primarily influenced by its metal constituents and crystal structure. First, specific metal elements, such as Sn, exhibit relatively high metal–hydrogen bond dissociation energies (BDEs) that enhance hydrogen bonding stability and suppress hydrogen-related defects by forming energetically favorable substitutional sites around the metal atoms [18]. By contrast, previous studies have reported that although H_2 annealing accelerates oxygen vacancy formation in OSs because of the reducing nature of hydrogen, the incorporation of the Si, which exhibits strong metal–oxygen bonding, effectively suppresses oxygen vacancy generation and preserves semiconducting behavior, even under high-temperature H_2 environments [19]. Second, molecular dynamics simulations and hybrid density functional theory calculations have demonstrated that the hydrogen defect formation energy of amorphous and crystalline In–oxide systems strongly depends on the hydrogen bonding configuration and location. In particular, grain boundary regions have been identified as structurally vulnerable sites with lower hydrogen defect formation energies [20]. Despite these insights, studies that include a systematic comparison of the relative dominance of hydrogen resistance factors in different OSs remain limited, and the behaviors of OSs in the high-temperature hydrogen environments relevant to the thermal budget of DRAM fabrication processes have not been evaluated.

Therefore, this study systematically analyzed the relative dominance of hydrogen resistance factors in ALD-fabricated OSs by evaluating various binary, ternary, and quaternary oxide film specimens with controlled metal compositions and crystallinities. Comparing the physical and electrical property changes of these films determined that Sn is the most effective metal element for imparting hydrogen resistance and provides amorphous structures exhibiting hydrogen stabilities superior to their crystalline counterparts. Based on these findings, the characteristics of an amorphous In–Sn–Ga–O (ITGO) film comprising an In:Sn:Ga atomic ratio of 1:1:1 at.% were investigated and compared with those of a conventional amorphous In–Ga–Zn–O (IGZO) film comprising an In:Ga:Zn ratio of 1:1:1 at.%. The ITGO film, in conjunction with a field-effect transistor (FET) incorporating this material, exhibited substantially enhanced hydrogen stability up to 600°C under ambient hydrogen conditions. Therefore, this study provides insights informing the material design of OS channels with excellent stability in high-temperature and hydrogen-rich conditions to enable their application in 3D DRAM cell transistors.

2 | Results and Discussion

As shown in Figure 1, the hydrogen tolerances of the considered binary oxide films (In_2O_3, Ga_2O_3, ZnO, and SnO_2) were first evaluated by comparing the changes in their physical and electrical properties after annealing in an ambient hydrogen atmosphere. As shown by the XRD patterns in Figure 1a, the four oxide films exhibited distinct crystal structures following pre-annealing at 400°C in air: In_2O_3 exhibited a cubic bixbyite phase, Ga_2O_3 remained amorphous, ZnO exhibited a hexagonal wurtzite structure, and SnO_2 exhibited a tetragonal rutile phase. The physical stabilities of these binary oxides under hydrogen exposure were assessed as shown in Figure 1b, which summarizes the film thickness variation measured by SE after annealing at 400°C, 500°C, and 600°C in hydrogen, conditions hereafter denoted as "H_2 400°C," "H_2 500°C," and "H_2 600°C," respectively. The measured film thickness was normalized relative to that obtained in the pristine state, which was defined as the corresponding specimen after pre-annealing at 400°C in air. The Ga_2O_3 film exhibited the highest stability with a negligible thickness change of less than 1%, even after annealing at H_2 600°C. By contrast, apparent damage was observed in the In_2O_3 film beginning at H_2 400°C, in the ZnO film beginning at H_2 500°C, and in the SnO_2 film beginning at H_2 600°C, when the film thickness became not detectable (N/D).

The origin of the observed film degradation was investigated by conducting XPS surface analyses of the In_2O_3, ZnO, and SnO_2 films annealed at H_2 600°C; the results are presented in Figure S1. Figure S1a shows the In 3d spectrum for the In_2O_3 film, Sn 3d spectrum for the SnO_2 film, and Zn 2p spectrum for the ZnO film. The In 3d and Sn 3d peaks remained consistent with oxidation states +3 and +4, respectively, with no prominent peak shifts, suggesting that reduction to metallic states and metal precipitation were unlikely; by contrast, the Zn 2p signal was observed close to the noise level. The surface compositions shown in Figure S1b indicate that H_2 annealing substantially decreased the metal fractions to 2.8% for In, 18.8% for Sn, and near zero for Zn; these decreases were accompanied by the appearance of signals from the Si substrate. Collectively, these results indicate that film etching occurred, which is consistent with previous reports describing high-temperature hydrogen reduction and etching of OS films via the formation of volatile hydride species [15].

Figure 1c,d presents the carrier concentration (n_e) and Hall mobility (μ_{Hall}) values obtained via Hall effect measurements of

2199160x, 2026, 18, Downloaded from https://advanced.onlinelibrary.wiley.com/doi/10.1002/aelm.70575 by Hanyang University Library, Wiley Online Library on [12/10/2026]. See the Terms and Conditions (https://onlinelibrary.wiley.com/terms-and-conditions) on Wiley Online Library for rules of use; OA articles are governed by the applicable Creative Commons License

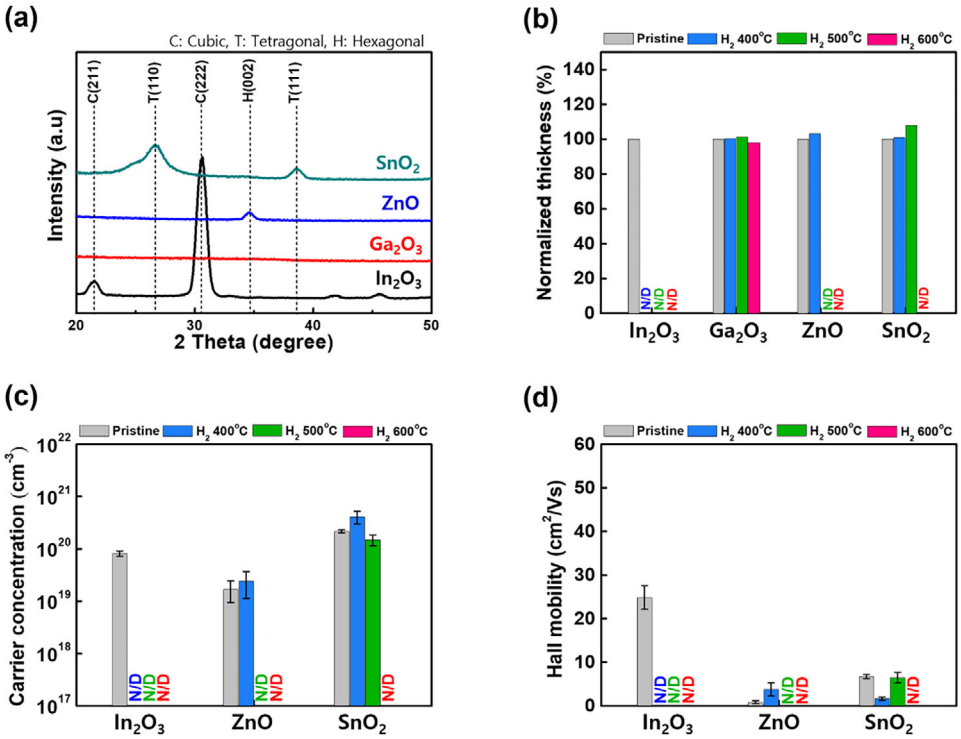

FIGURE 1 | (a) XRD patterns of In_2O_3, Ga_2O_3, ZnO, and SnO_2 annealed at 400°C. (b) Normalized film thickness, (c) n_e, and (d) μ_{Hall} of pristine and H_2-annealed (400°C–600°C) binary oxide films.

the pristine and H_2-annealed films. However, electrical characteristics could not be obtained for the etched specimens; accordingly, the results for these specimens were denoted as N/D. Because film loss reduced the number of comparable specimens, the electrical data were insufficient to establish a clear trend in hydrogen tolerance. Nevertheless, the physical stability assessed based on the observed thickness retention indicated that the hydrogen tolerance of the binary oxides increased from In_2O_3 to ZnO, SnO_2, and Ga_2O_3. However, this trend likely reflects the combined influence of both the metal constituent and crystal structure because all four oxides differed in both cation chemistry and structural phase, limiting attribution of the observed differences to a single dominant factor. In addition, because binary oxides often behave as conductors or insulators, the investigation must be extended to include multicomponent oxide systems before such materials can be practically applied as semiconductor channels.

Therefore, the influence of metal constituents on hydrogen tolerance was evaluated using four ternary oxide systems. As illustrated in Figure 2a, these oxides comprised In–Ga–O (IGO), In–Sn–O (ITO), Ga–Sn–O (GTO), and In–Zn–O (IZO) with fixed cation ratios of 1:1 at.% to exclude the influence of cation composition. The XRD patterns in Figure S2 indicates that none of the ternary oxides prepared with a 1:1 cation ratio exhibited detectable diffraction peaks after annealing at 400°C in air, confirming that they remained in the amorphous phase. This experimental design enabled the comparison of hydrogen tolerance as a function of metal species while minimizing the influence of crystallinity. Additionally, fixing one cation at 50 at.% minimized the influence of the shared element, facilitating direct assessment of the effects of the remaining metal constituent on hydrogen tolerance.

Figure 2b summarizes the normalized thickness variation of the ternary oxide films after H_2 annealing at 400°C–600°C. The IZO film was physically stable up to H_2 400°C, but was fully etched at H_2 500°C and above, resulting in an N/D thickness. The IGO film exhibited an approximately 7% reduction in thickness at H_2 500°C, reflecting higher stability than the IZO, and became fully etched at H_2 600°C. The GTO film exhibited stable thickness retention within 0.5% up to H_2 500°C and was fully etched at H_2 600°C. The ITO film exhibited an approximately 4% decrease in thickness at H_2 600°C, reflecting the highest physical stability among the considered ternary oxides. Therefore, the measured thickness retention values indicated that resistance to hydrogen-induced reduction increased from Zn to Ga, In, and Sn. This trend can be explained by considering the reported film density and bond strength values. For example, the density of SnO_2 (6.48 g/cm^3) is higher than that of ZnO (5.23 g/cm^3), which can reduce the hydrogen transport within the film [21, 22]. In addition, the reported oxygen BDE values for Sn–O (528 kJ/mol) are higher than those for Zn–O (250 kJ/mol), which can increase the energetic barrier for hydrogen reduction and the subsequent formation of volatile hydride species via the reaction $SnO_2 + H \rightarrow SnH_4$ (g) + H_2O (g) compared with ZnO + H → ZnH_2 (g) + H_2O (g) [23].

Figure 2c–f presents the n_e and μ_{Hall} values for the pristine and H_2-annealed ternary oxides, in conjunction with the corresponding changes relative to the pristine state, expressed as $\Delta\log(n_e)$ and $\Delta\mu_{Hall}$. The fully etched specimens exhibited no measurable electrical characteristics and are denoted as N/D accordingly. In terms of $\Delta\log(n_e)$, the stability against hydrogen-induced change at H_2 400°C increased from IZO (+1.60 decades) to IGO (+0.77 decades), ITO (+0.30 decades), and GTO (−0.14 decades), and

21991160x, 2026, 18, Downloaded from https://advanced.onlinelibrary.wiley.com/doi/10.1002/aelm.70575 by Hanyang University Library, Wiley Online Library on [12/10/2026]. See the Terms and Conditions (https://onlinelibrary.wiley.com/terms-and-conditions) on Wiley Online Library for rules of use; OA articles are governed by the applicable Creative Commons License

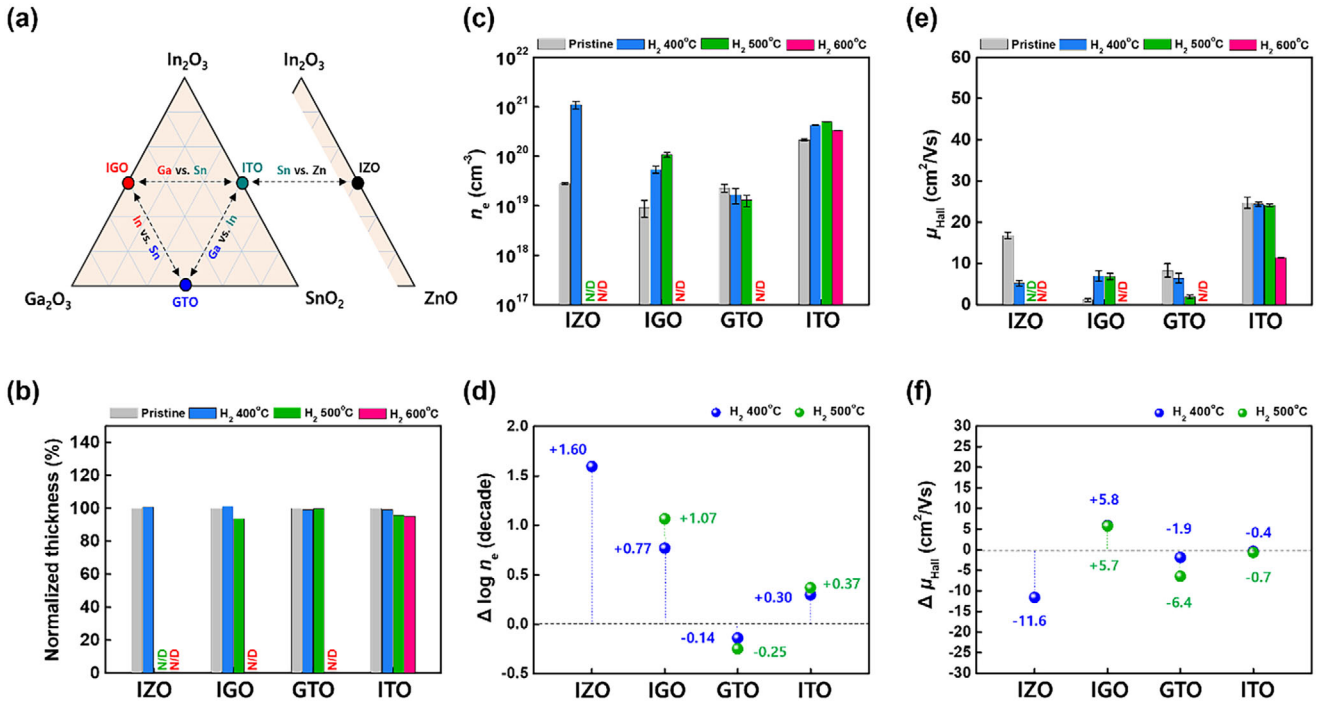

FIGURE 2 | (a) Cation composition maps of IZO, IGO, GTO, and ITO evaluated to compare the effects of different metal elements. (b) Normalized film thickness, (c) n_e, (d) $\Delta\log(n_e)$, (e) μ_{Hall}, and (f) $\Delta\mu_{Hall}$ of pristine and H_2-annealed (400°C–600°C) ternary oxide films.

that at H_2 500°C increased from IGO (+1.07 decades) to ITO (+0.37 decades), and GTO (−0.25 decades). In terms of $\Delta\mu_{Hall}$, the stability against hydrogen-induced change at H_2 400°C increased from IZO (−11.6 cm^2/Vs) to IGO (+5.8 cm^2/Vs), GTO (−1.9 cm^2/Vs), and ITO (−0.4 cm^2/Vs), and that at H_2 500°C increased from GTO (−6.4 cm^2/Vs) to IGO (+5.7 cm^2/Vs), then ITO (−0.7 cm^2/Vs). These results suggest that the stability of hydrogen-induced electrical property changes generally increased from Zn to In and Ga, then Sn.

The comparatively smaller hydrogen-induced electrical variation in the Sn-containing oxide films can be discussed in terms of hydrogen bonding configuration. Because the reported BDE for Sn–H (264 kJ/mol) is higher than that for Zn–H (86 kJ/mol), hydrogen is more likely to be stabilized near Sn sites [23]. This stabilization can increase the fraction of substitutional hydrogen states with deeper electronic levels relative to that of interstitial hydrogen or O—H bonding, which act as shallow donors. Collectively, these results suggest that the hydrogen tolerance of an OS is predominantly determined by its constituent metal species and indicate that Sn incorporation can effectively improve both physical and electrical resistance under high-temperature ambient hydrogen conditions.

However, the elemental hydrogen resistance trend derived from the 1:1 at.% ternary oxides differed substantially from that observed for the corresponding binary oxides in Figure 1. As shown in Figure 1b, the physical hydrogen tolerance increased from In_2O_3 (cubic) to ZnO (hexagonal), SnO_2 (tetragonal), and Ga_2O_3 (amorphous), suggesting that crystal structure is a dominant factor exerting an influence comparable to or even exceeding that of the metal species. Therefore, the influence of crystallinity was examined using phase-engineered IGO and ITO films prepared by tuning their cation compositions; this is a common approach for controlling crystallization. As illustrated in Figure S3a, cubic IGO (c-IGO), amorphous IGO (a-IGO), cubic ITO (c-ITO), amorphous ITO (a-ITO), and tetragonal ITO (t-ITO) films were deposited and compared. The comparisons of $\Delta\log(n_e)$ in Figure S3b,d and $\Delta\mu_{Hall}$ in Figure S3c,e indicates that the amorphous phases consistently exhibited superior hydrogen resistance up to H_2 500°C; however, the concurrent variation in cation composition limited the ability of these comparisons to isolate the effect of crystallinity.

Therefore, crystallinity was further controlled by modifying the pre-annealing temperature while maintaining the same cation composition for each material. Specifically, ITO with In:Sn = 1:1 at.% and IGO with In:Ga = 2:1 at.% were pre-annealed at 400°C and 600°C in air, then evaluated prior to H_2 annealing. Figure 3a shows the XRD patterns of the ITO and IGO films according to the applied pre-annealing temperature. Both films remained amorphous after pre-annealing at 400°C, and were denoted as a-ITO and a-IGO accordingly. By contrast, both films crystallized into the cubic bixbyite structure after pre-annealing at 600°C, which is consistent with the observed behavior of In_2O_3, yielding c-ITO and c-IGO. Notably, c-ITO exhibited a randomly oriented polycrystalline character, whereas c-IGO exhibited a preferred orientation dominated by cubic (400) reflection. Figure 3b compares the normalized thickness variation of ITO and IGO films comprising amorphous and crystalline phases after H_2 annealing at 400°C–600°C. The a-ITO film exhibited only a marginal decrease in thickness of approximately 4% at H_2 600°C, whereas the c-ITO film was fully etched at H_2 600°C, indicating markedly reduced physical stability after crystallization. Similarly, the a-IGO film exhibited a 28% thickness reduction at H_2 600°C, whereas the c-IGO film was fully etched under the same

21999160x, 2026, 18, Downloaded from https://advanced.onlinelibrary.wiley.com/doi/10.1002/aelm.70575 by Hanyang University Library, Wiley Online Library on [12/10/2026]. See the Terms and Conditions (https://onlinelibrary.wiley.com/terms-and-conditions) on Wiley Online Library for rules of use; OA articles are governed by the applicable Creative Commons License

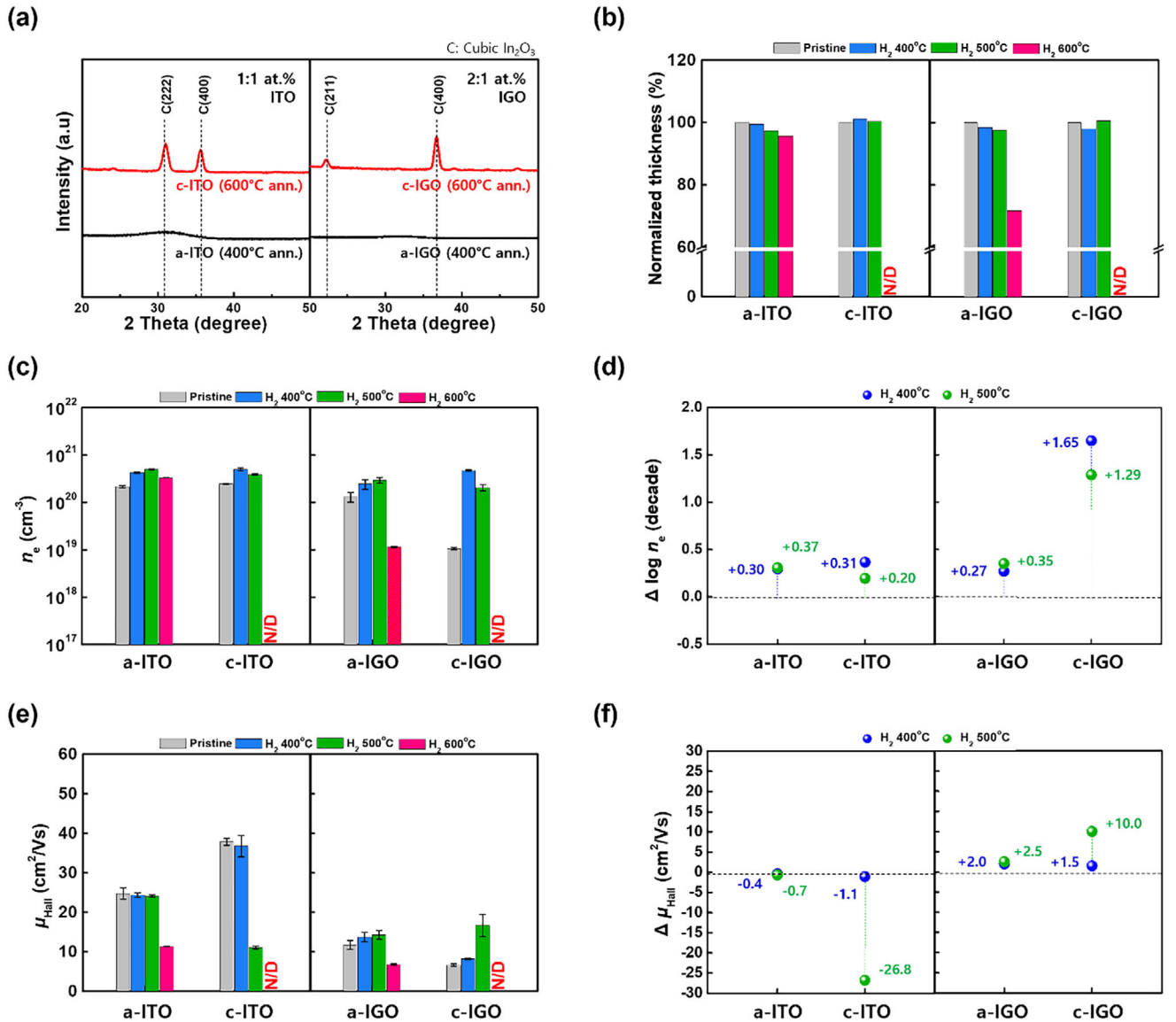

FIGURE 3 | (a) XRD patterns of ITO (In:Sn = 1:1 at.%) and IGO (In:Ga = 2:1 at.%) films pre-annealed at 400°C and 600°C. (b) Normalized film thickness, (c) n_e, (d) $\Delta\log(n_e)$, (e) μ_{Hall}, and (f) $\Delta\mu_{Hall}$ of pristine and H_2-annealed (400°C–600°C) a-/c-ITO and a-/c-IGO films.

conditions. The degraded physical stabilities of the crystalline films compared with those of their amorphous counterparts can be attributed to grain boundary effects. Grain boundaries provide rapid diffusion pathways for hydrogen transport into the film as well as undercoordinated sites that facilitate hydrogen-induced reduction reactions, thereby promoting film etching under high-temperature ambient hydrogen conditions [24].

Figure 3c,e presents the n_e and μ_{Hall} values for the amorphous and crystalline ITO and IGO films in the pristine and H_2-annealed conditions, and Figure 3d,f summarize the corresponding changes relative to the pristine state in terms of $\Delta\log(n_e)$ and $\Delta\mu_{Hall}$. No electrical characteristics were detected in either of the crystalline films annealed at H_2 600°C owing to the occurrence of complete film etching. The $\Delta\log(n_e)$ values for the a-ITO and c-ITO films exhibited only minor differences at H_2 400°C and H_2 500°C, remaining near 0.3 decades. By contrast, the $\Delta\log(n_e)$ values for the IGO films exhibited a pronounced crystallinity dependence. At H_2 400°C, c-IGO exhibited a substantially larger increase in n_e than that of a-IGO, with a $\Delta\log(n_e)$ value of +1.65 decades for c-IGO and +0.27 decades for a-IGO. A similar trend was observed at H_2 500°C, when the $\Delta\log(n_e)$ value for c-IGO was +1.29 decades and that for a-IGO was +0.35 decades. Comparing the $\Delta\mu_{Hall}$ values at H_2 500°C, the amorphous phases consistently exhibited greater stability than the crystalline phases, as indicated by the difference between c-ITO (−26.8 cm^2/Vs) and a-ITO (−0.7 cm^2/Vs) and between c-IGO (+10.0 cm^2/Vs) and a-IGO (+2.5 cm^2/Vs). Collectively, these results suggest that the hydrogen stability of an amorphous film is superior to that of a crystalline film in terms of both physical integrity and electrical properties. This difference can be attributed to grain boundary-assisted hydrogen diffusion as well as the reduced formation energy of hydrogen-related defects at the grain boundaries in the crystalline network compared with that in the amorphous network [20, 24]. Grain boundaries act as structural weak points for hydrogen tolerance, highlighting the inherent advantages

2199160x, 2026, 18, Downloaded from https://advanced.onlinelibrary.wiley.com/doi/10.1002/aelm.70575 by Hanyang University Library, Wiley Online Library on [12/10/2026]. See the Terms and Conditions (https://onlinelibrary.wiley.com/terms-and-conditions) on Wiley Online Library for rules of use; OA articles are governed by the applicable Creative Commons License

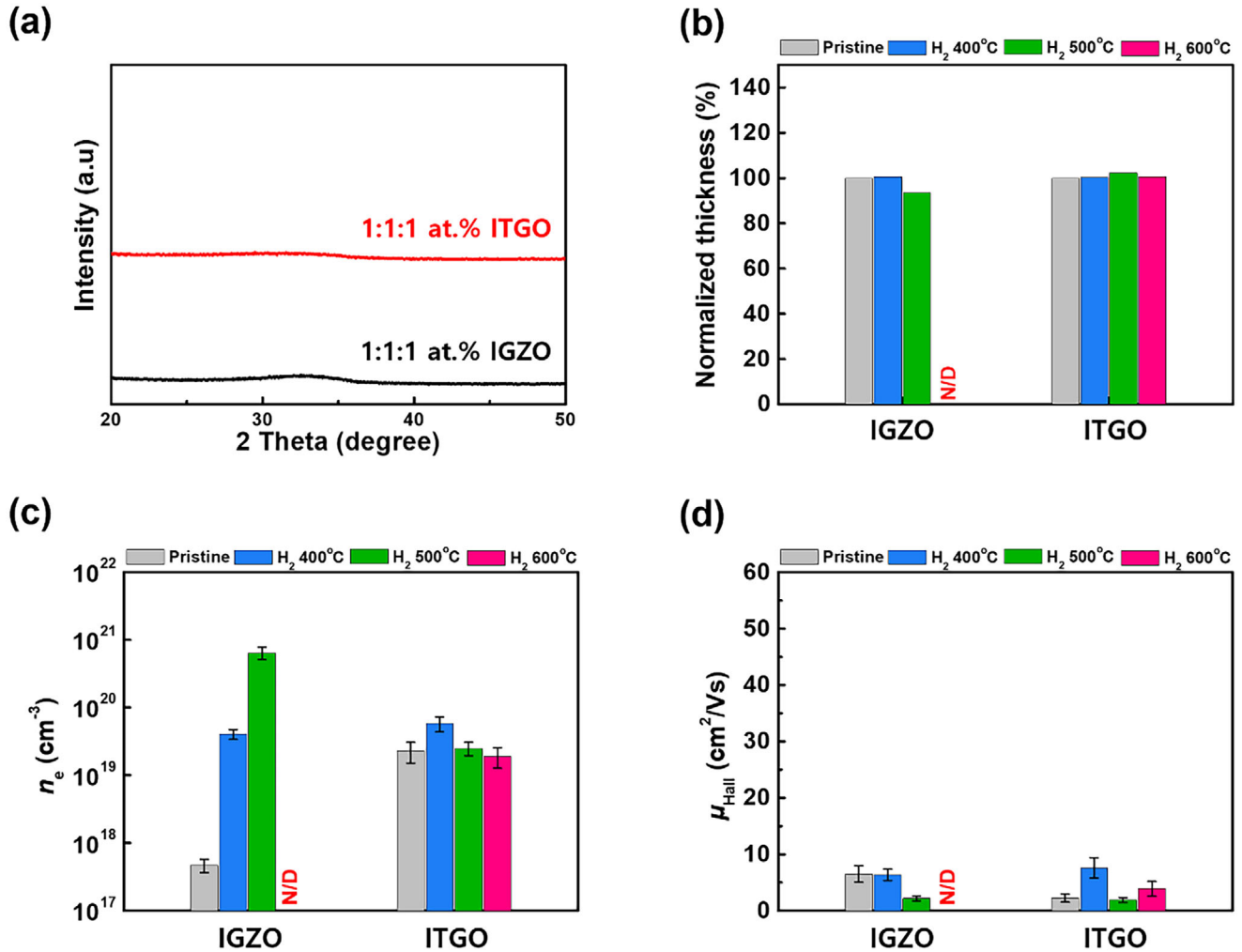

FIGURE 4 | (a) XRD patterns of IGZO (In:Ga:Zn = 1:1:1 at.%) and ITGO (In:Sn:Ga = 1:1:1 at.%) pre-annealed at 400°C. (b) Normalized film thickness, (c) n_e, and (d) μ_{Hall} of pristine and H_2-annealed (400°C–600°C) quaternary oxide films.

of amorphous OSs for applications subject to high-temperature ambient hydrogen processing.

Figure 4 extends the evaluation of hydrogen tolerance to quaternary oxide semiconductors and compares an optimized amorphous Sn-containing ITGO comprising In:Sn:Ga = 1:1:1 at.% with a conventional IGZO comprising In:Ga:Zn = 1:1:1 at.%. Figure 4a shows the XRD patterns of the IGZO and ITGO films, both of which exhibited amorphous phases, thereby excluding the influence of crystallinity. Figure 4b presents the normalized thickness variation of the films after H_2 annealing at 400°C–600°C. Clear physical degradation in the IGZO was observed at H_2 500°C and above; this was accompanied by an approximately 7% reduction in thickness, and the film was fully etched at H_2 600°C. By contrast, the ITGO exhibited a negligible thickness change of less than 1% up to H_2 600°C.

The temperature-dependent hydrogen stability of electrical properties is summarized in terms of n_e and μ_{Hall} in Figure 4c,d, respectively. For the IGZO film, n_e increased abruptly by more than three orders of magnitude from 4.7×10^{17} cm^{-3} in the pristine state to 6.4×10^{20} cm^{-3} at H_2 500°C, whereas μ_{Hall} decreased from 6.5 to 2.2 cm^2/Vs; no electrical characteristics were detected at H_2 600°C because the film was etched. By contrast, the ITGO film exhibited only minor changes in n_e from 2.3×10^{19} to 1.9×10^{19} cm^{-3} and μ_{Hall} from 2.2 to 3.9 cm^2/Vs from the pristine state up to H_2 600°C.

The superior physical and electrical hydrogen tolerance of the ITGO film over that of the IGZO film can be primarily attributed to their different metal constituents. Because both films remained amorphous and shared identical cation fractions of In and Ga (33 at.%), the enhanced hydrogen tolerance of ITGO is likely associated with the substitution of Zn with Sn. This conclusion is consistent with the elemental dependence observed in the ternary oxide systems and suggests that the key factors governing hydrogen tolerance can be extended from ternary to quaternary oxide compositions when designing OS channels.

Next, the electrical characteristics and hydrogen tolerances of IGZO- and ITGO-channel inverted staggered FETs fabricated using the process flow shown in Figure 5a were evaluated. The transfer curves and key device parameters of the pristine and H_2-annealed (400°C–600°C) IGZO FETs are summarized in Figure 5b,c, and the corresponding results for the ITGO FETs are presented in Figure 5d,e. The IGZO FET exhibited

2199160x, 2026, 18, Downloaded from https://advanced.onlinelibrary.wiley.com/doi/10.1002/aelm.70575 by Hanyang University Library, Wiley Online Library on [12/10/2026]. See the Terms and Conditions (https://onlinelibrary.wiley.com/terms-and-conditions) on Wiley Online Library for rules of use; OA articles are governed by the applicable Creative Commons License

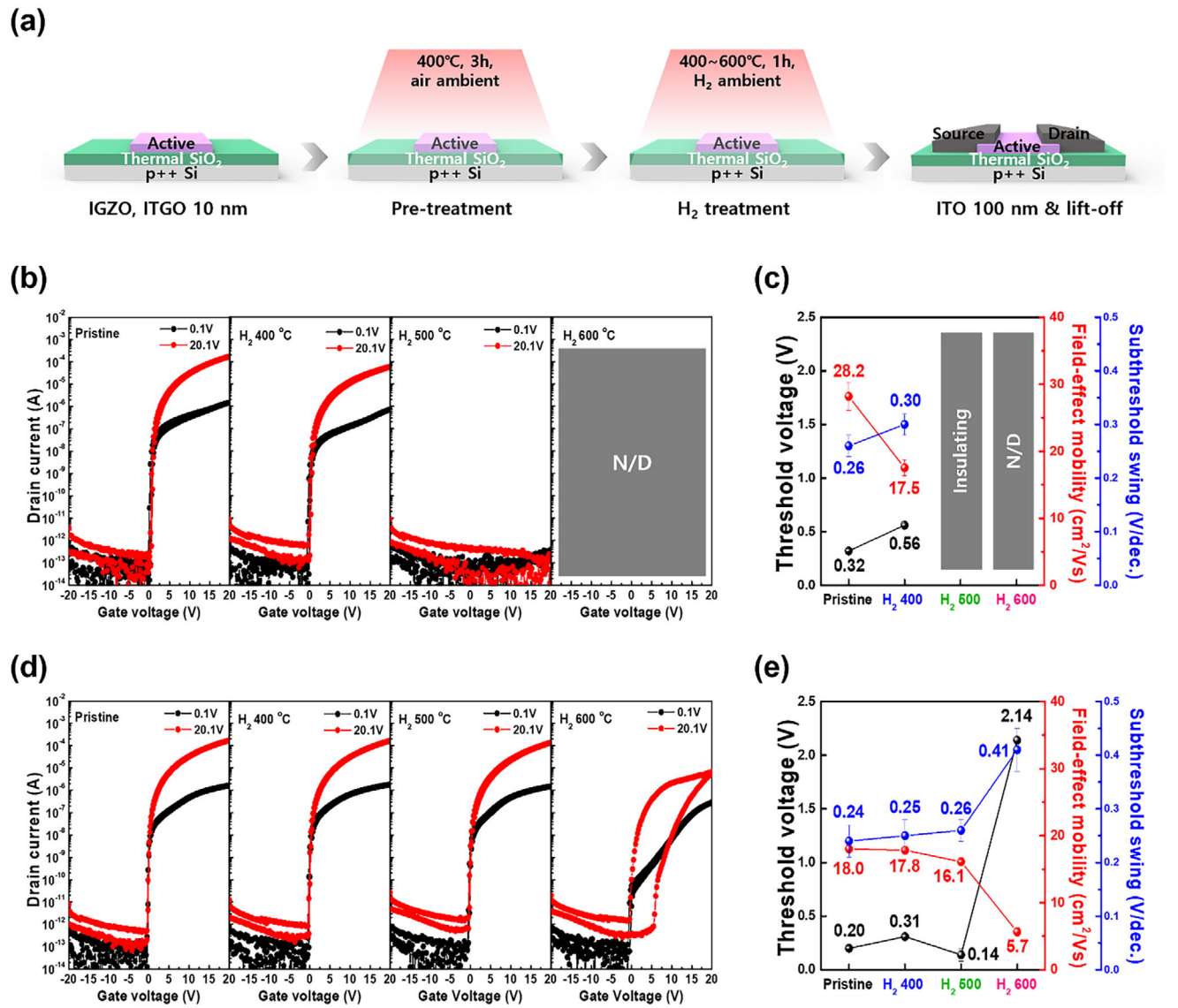

FIGURE 5 | (a) Schematic of the process used to fabricate inverted staggered IGZO and ITGO FETs. Transfer curves measured at $V_D = 0.1$ and 20.1 V for the pristine and H_2-annealed (400°C–600°C) (b) IGZO and (d) ITGO FETs, with the corresponding extracted electrical parameters (V_{TH}, μ_{FE}, *SS*) shown in (c) and (e), respectively.

normal switching characteristics under the pristine and H_2 400°C conditions. At H_2 500°C, it exhibited insulating behavior, and device fabrication was unfeasible at H_2 600°C owing to severe channel etching. The H_2 400°C IGZO FET exhibited a clear onset of degradation when compared with the pristine IGZO FET, with a field-effect mobility (μ_{FE}) decreasing from 28.2 to 17.5 cm^2/Vs and a subthreshold swing (*SS*) increasing from 0.26 to 0.30 V/decade. This degradation became more severe at H_2 500°C, which is consistent with a substantial reduction observed in IGZO channel conductivity. By contrast, the ITGO FET maintained switching characteristics up to H_2 600°C. Only minor differences between the electrical characteristics of the pristine and H_2 500°C ITGO FETs were observed, with μ_{FE} decreasing from 18.0 to 16.1 cm^2/Vs and *SS* increasing from 0.24 to 0.26 V/decade. However, the H_2 600°C ITGO FET exhibited the onset of device degradation, with a V_{TH} of 2.14 V, a reduced μ_{FE} of 5.7 cm^2/Vs, and an increased *SS* of 0.41 V/decade.

These device-level results are consistent with the film-level trends, confirming that the ITGO exhibits significantly enhanced hydrogen tolerance compared with IGZO. Notably, compared with the film-level electrical properties shown in Figure 4, the onset of degradation in the FETs was observed at a lower temperature range for both the IGZO and ITGO. This difference can be attributed to the smaller channel area of the FETs (40 × 20 μm) compared with the evaluation area used for film-level measurements (2 × 2 cm), which can amplify the impact of surface-related reactions and potentially accelerate hydrogen-induced degradation. In particular, the insulating behavior observed in the H_2 500°C annealed IGZO FET may originate from the severe hydrogen-induced etching of the 10-nm-thick channel, which can reduce the effective channel thickness to the sub-nanometer regime where quantum confinement becomes significant, thereby suppressing the carrier concentration. In addition, hydrogen-induced interfacial changes that are challenging to capture via SE and Hall effect measurements, such as changes

21991160x, 2026, 18, Downloaded from https://advanced.onlinelibrary.wiley.com/doi/10.1002/aelm.70575 by Hanyang University Library, Wiley Online Library on [12/10/2026]. See the Terms and Conditions (https://onlinelibrary.wiley.com/terms-and-conditions) on Wiley Online Library for rules of use; OA articles are governed by the applicable Creative Commons License

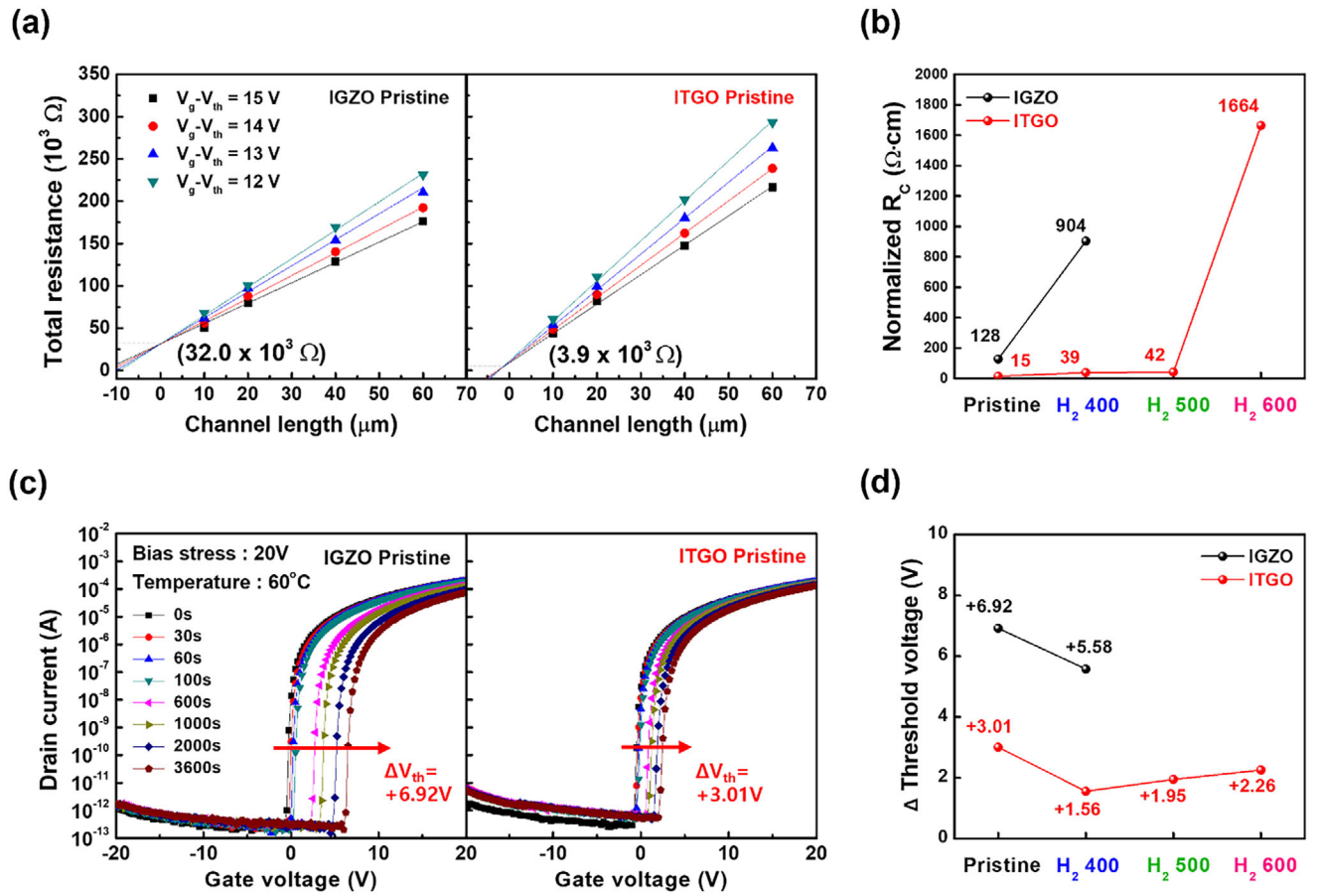

FIGURE 6 | (a) Total resistance as a function of channel length with a fixed channel width of 40 μm and (c) transfer curves under PBTS (2 MV/cm at 60°C for 1 h) for pristine IGZO and ITGO FETs. (b) Width-normalized R_C and (d) ΔV_{TH} under PBTS for pristine and H_2-annealed (400°C–600°C) IGZO and ITGO FETs.

in the states of the contact or gate insulator interfaces, may have contributed to the observed device-level degradation [25, 26]. Further evaluations are required to clarify the contributions of such changes.

Therefore, the transmission line method (TLM) was employed to quantitatively assess the hydrogen-induced variations in FET contact resistance. The width-normalized contact resistance (R_C) was extracted using the TLM by linearly fitting the total resistance as a function of channel length and extrapolating the intercept at zero channel length. Figure 6a shows representative TLM fittings for the pristine IGZO and ITGO FETs, and Figure 6b summarizes the R_C values for the pristine and H_2-annealed FETs. The width-normalized R_C for the IGZO FET substantially increased from 128 Ω cm in the pristine state to 904 Ω cm at H_2 400°C. By contrast, the ITGO FET exhibited a substantially lower R_C of 15 Ω cm in the pristine state, which is likely the result of a reduced Schottky barrier at the ITO electrode interface owing to the relatively higher Fermi level of ITGO [27, 28]. The ITGO FET exhibited only a minor increase in R_C from 15 in the pristine condition to 42 Ω cm at H_2 500°C, whereas R_C increased abruptly to 1664 Ω cm at H_2 600°C, clearly indicating the onset of degradation. The temperature range in which R_C degradation became pronounced corresponds to the regime in which the reduction in μ_{FE} accelerated, as shown in Figure 5c,e. These results suggest that device degradation under high-temperature ambient hydrogen conditions is dominated by an increase in the contact resistance rather than by changes in the bulk channel conductivity.

Furthermore, the hydrogen-induced stability of the gate insulator interface was evaluated by analyzing the threshold voltage shift (ΔV_{TH}) under positive bias temperature stress (PBTS) at 60°C and 2 MV/cm for 1 h. Figure 6c shows the transfer curves for the pristine IGZO and ITGO FETs as a function of PBTS time, and Figure 6d and Figure S4 summarizes the ΔV_{TH} values for the pristine condition and after H_2 annealing at 400°C–600°C. For the IGZO FET, the ΔV_{TH} under PBTS was +6.92 V in the pristine state and marginally decreased to +5.58 V at H_2 400°C. For the ITGO FET, ΔV_{TH} was +3.01 V in the pristine state, which is lower than that for the IGZO FET under the same condition. This improvement can be attributed to the reduced density of oxygen-related defects and electron trapping, which are potentially associated with the higher oxygen bond strength of Sn compared with that of Zn [17]. After H_2 annealing, the ITGO FET exhibited ΔV_{TH} values of +1.56 V at H_2 400°C, +1.95 V at H_2 500°C, and +2.26 V at H_2 600°C; these values are consistently lower than those for the corresponding IGZO FETs. Previous studies have suggested that hydrogen can improve FET reliability via interface trap passivation under moderate conditions [29]. However, reduction reactions near the interface can be activated under high-temperature

2199160x, 2026, 18, Downloaded from https://advanced.onlinelibrary.wiley.com/doi/10.1002/aelm.70575 by Hanyang University Library, Wiley Online Library on [12/10/2026]. See the Terms and Conditions (https://onlinelibrary.wiley.com/terms-and-conditions) on Wiley Online Library for rules of use; OA articles are governed by the applicable Creative Commons License

hydrogen exposure, increasing interface roughness and trap density, which can degrade contact resistance and PBTS reliability [30, 31]. Overall, this comparative analysis of hydrogen tolerance factors indicates that amorphous ITGO represents a promising channel material for replacing conventional IGZO in DRAM applications. However, although the bulk properties of ITGO remain relatively stable during H_2 annealing up to 600°C, device-level degradation was observed in conjunction with deterioration at the contact and gate insulator interfaces. Therefore, ensuring hydrogen tolerance at OS interfaces should be investigated in future research.

3 | Conclusion

This study systematically investigated the high-temperature hydrogen tolerance of OSs to elucidate how their constituent metal species and crystallinity govern their physical integrity and electrical stability. Comparing amorphous ternary oxide films sharing a fixed 1:1 at.% cation ratio indicated that the incorporation of Sn simultaneously improved thickness retention and stabilized carrier concentration (n_e) and Hall mobility (μ_{Hall}) after H_2 annealing. Furthermore, a direct comparison of amorphous and crystalline phase films with identical cation compositions indicated that the reduced hydrogen tolerance of the latter can be attributed to grain boundary effects that promote hydrogen transport and facilitate the formation of hydrogen-related defects. Based on these findings, an amorphous ITGO film was designed and benchmarked against conventional IGZO film. The thickness variation of the ITGO film remained within 1% after H_2 annealing up to 600°C and exhibited only limited changes in n_e and μ_{Hall}, reflecting robust bulk channel stability under high-temperature ambient hydrogen conditions. Furthermore, an FET-level evaluation confirmed that ITGO preserves switching characteristics and provides substantially enhanced hydrogen tolerance after H_2 annealing up to 600°C compared with that of IGZO. The results of TLM and PBTS analyses further revealed that device degradation during high-temperature hydrogen exposure was driven by the degradation of the contact and gate insulator interface stability rather than changes in bulk channel conductivity. Collectively, the results of this study establish guidelines for the design of hydrogen-process-compatible oxide channels employing amorphous Sn-containing compositions and provide a foundation for realizing OS channels that remain stable in high-temperature hydrogen environments.

4 | Experimental Section/Methods

4.1 | Film and FET Fabrication Methods

The thin oxide films evaluated in this study were deposited using a rectangular (4 in wafer scale) lateral gas-flow-type thermal ALD reactor (Mini-ALD, Nexusbe). Four metal precursors, (3-dimethylaminopropyl)dimethylindium (DADI) and dimethyl[N-(tert-butyl)−2-methoxy-2-methylpropan-1-amine]gallium (DMGON) (Hansol Chemical Co., Limited), diethylzinc (DEZ), and bis(dimethylamino)dimethyltin (BDMADMSn), were applied using ozone (210 g/m^3) as the oxidant. The DMGON and BDMADMSn precursors were heated to 45°C, whereas the DADI and DEZ precursors were maintained at 30°C; Ar gas (99.999%) served as the carrier and purging gas at a flow rate of 110 sccm.

Inverted staggered IGZO and ITGO FETs were fabricated using a thermally grown SiO_2 100 nm/p^{++}-doped silicon wafer as the gate insulator and electrode. The IGZO and ITGO channel layers were deposited to achieve a thickness of 10 nm using ALD, followed by channel patterning employing lithography and wet-etching processes. Pre-annealing was subsequently performed at 400°C for 3 h in air, followed by H_2 annealing at 400°C, 500°C, or 600°C for 1 h in an ambient hydrogen environment (forming gas, H_2:N_2 = 4:96%). Radiofrequency sputtering was employed to deposit In–Sn–O (ITO) as the source and drain electrodes, which were patterned via lithography and lift-off processes. The FET evaluation was conducted using a Keithley 4200 semiconductor parameter analyzer in a dark and vacuum environment with channel dimensions of 40 μm width and 20 μm length.

4.2 | Analysis Methods

Spectroscopic ellipsometry (SE; Elli-SE(UV)-FM8, Ellipso Technology) was employed to measure the film thickness; the deposited thin films consistently exhibited a thickness of 30 nm. The electrical properties of each thin film, including carrier concentration (n_e) and Hall mobility (μ_{Hall}), were investigated using a Hall effect measurement system (HMS-5500/AHT55T5, Ecopia) equipped with a 0.56 T permanent magnet. The raw Hall measurement data for the carrier concentration (n_e) and Hall mobility (μ_{Hall}) of each material as a function of H_2 annealing temperature are summarized in Tables S1 and S2, respectively. The changes after H_2 annealing were calculated as $\Delta \log n_e = \log(n_{ann.}) - \log(n_{pristine})$ and $\Delta\mu_{Hall} = \mu_{ann.} - \mu_{pristine}$, respectively. The cation ratios of the ternary and quaternary oxide films were analyzed using x-ray fluorescence (XRF; Thermo Fisher Scientific Co.). The crystallinity of each thin film was determined using grazing-incidence x-ray diffraction (XRD; Smartlab, Rigaku). The chemical bonding state and composition of each film specimen were analyzed via x-ray photoelectron spectroscopy (XPS; K-alpha+, Thermo Fisher Scientific Co.).

Author Contributions

Seong-Hwan Ryu: conceptualization, methodology, data curation, writing – review and editing, writing – original draft, formal analysis. **Sun Myung Lee**: methodology, data curation, writing – original draft, writing – review and editing. **Kwang-Hee Lee**: resources, writing – review and editing, writing – original draft, funding acquisition, data curation. **Jee-Eun Yang**: data curation, resources, writing – review and editing, writing – original draft, funding acquisition. **Sangwook Kim**: writing – original draft, writing – review and editing, funding acquisition, resources, supervision. **Jin-Seong Park**: supervision, conceptualization, validation, investigation, writing – review and editing, writing – original draft.

Acknowledgements

This study was supported by Samsung Electronics, the National Research Foundation of Korea (NRF) grant funded by the Korea government (MSIT) (RS-2023-00260527), the Korea Institute for Advancement of Technology (KIAT) grant funded by the Korean Ministry of Trade, Industry, and Energy (MOTIE) (RS-2024-00410066), the Nano & Material Technol-

2199160x, 2026, 18, Downloaded from https://advanced.onlinelibrary.wiley.com/doi/10.1002/aelm.70575 by Hanyang University Library, Wiley Online Library on [12/10/2026]. See the Terms and Conditions (https://onlinelibrary.wiley.com/terms-and-conditions) on Wiley Online Library for rules of use; OA articles are governed by the applicable Creative Commons License

ogy Development Program through the National Research Foundation of Korea (NRF) funded by Ministry of Science and ICT (RS-2025-25442273), the Technology Innovation Program (or Industrial Strategic Technology Development Program) (RS-2025-25454815) funded by the Ministry of Trade Industry & Energy (MOTIE, Korea), and the Technology Innovation Program (RS-2025-02308064) funded by the Ministry of Trade Industry & Energy (MOTIE, Korea). This research was supported by the "Regional Innovation System & Education (RISE)" through the Seoul RISE Center, funded by the Ministry of Education (MOE) and the Seoul Metropolitan Government (2025-RISE-01-027-04).

Conflicts of Interest

The authors declare no conflicts of interest.

Data Availability Statement

The data that support the findings of this study are available in the supplementary material of this article.

References

1. Y. Fan, R. An, J. Tang, et al., "Monolithic 3D Integration as a Pathway to Energy-Efficient Computing and Beyond: From Materials and Devices to Architectures and Chips," *Current Opinion in Solid State and Materials Science* 33 (2024): 101199, https://doi.org/10.1016/j.cossms.2024.101199.

2. C.-H. Lee, S.-H. Ryu, T. Hwang, S.-H. Kim, Y.-S. Kim, and J.-S. Park, "Oxide Semiconductor for Advanced Memory Architectures: Atomic Layer Deposition, Key Requirement and Challenges," *Nano-Micro Letters* 18 (2026): 180, https://doi.org/10.1007/s40820-025-02013-7.

3. S.-K. Lu, H.-K. Huang, C.-L. Hsu, C.-T. Sun, and K. Miyase, "Retention-Aware Refresh Techniques for Reducing Power and Mitigation of Data Retention Faults in DRAM," *Journal of Electronic Testing* 35, no. 4 (2019): 485–495, https://doi.org/10.1007/s10836-019-05817-9.

4. J. Sheng, T. H. Hong, H. M. Lee, et al., "Amorphous IGZO TFT With High Mobility of ~70 cm^2 /(V s) via Vertical Dimension Control Using PEALD," *ACS Applied Materials & Interfaces* 11, no. 43 (2019): 40300–40309, https://doi.org/10.1021/acsami.9b14310.

5. R. Lu, S. Li, J. Lu, et al., "Homojunction Structure Amorphous Oxide Thin Film Transistors With Ultra-High Mobility," *Journal of Semiconductors* 44, no. 5 (2023): 52101, https://doi.org/10.1088/1674.

6. M. M. Billah, M. M. Islam, S. Priyadarshi, et al., "Multi-Channel, Amorphous Oxide Thin-Film Transistor Exhibiting High Mobility of 67 cm 2 V^{-1} s^{-1} and Excellent Stability," *Advanced Electronic Materials* 11, no. 8 (2025): 2400766, https://doi.org/10.1002/aelm.202400766.

7. K. Lai, Y. Liu, M. Li, et al., "Enhanced Mobility and Stability of Amorphous IZO TFTs with Homojunction Formation and Back-Channel Engineering," *IEEE Journal of the Electron Devices Society* 13 (2025): 997–1005, https://doi.org/10.1109/JEDS.2025.3598941.

8. Y. J. Baek, I. H. Kang, S. H. Hwang, et al., "Vertical Oxide Thin-Film Transistor With Interfacial Oxidation," *Scientific Reports* 12, no. 1 (2022): 3094, https://doi.org/10.1038/s41598-022-07052-3.

9. J. S. Hur, S. Lee, J. Moon, et al., "Oxide and 2D TMD Semiconductors for 3D DRAM Cell Transistors," *Nanoscale Horizons* 9, no. 6 (2024): 934–945, https://doi.org/10.1039/d4nh00057a.

10. T. Kamiya, K. Nomura, and H. Hosono, "Present Status of Amorphous In–Ga–Zn–O Thin-Film Transistors," *Science and Technology of Advanced Materials* 11, no. 4 (2010): 044305, https://doi.org/10.1088/1468-6996/11/4/044305.

11. H. Y. Noh, J. Kim, J.-S. Kim, M.-J. Lee, and H.-J. Lee, "Role of Hydrogen in Active Layer of Oxide-Semiconductor-Based Thin Film Transistors," *Crystals* 9, no. 2 (2019): 75, https://doi.org/10.3390/cryst9020075.

12. G. Li, A. Abliz, L. Xu, et al., "Understanding Hydrogen and Nitrogen Doping on Active Defects in Amorphous in-Ga-Zn-O Thin Film Transistors," *Applied Physics Letters* 112, no. 25 (2018): 253504, https://doi.org/10.1063/1.5032169.

13. Y. Lee, T. Nam, S. Seo, et al., "Hydrogen Barriers Based on Chemical Trapping Using Chemically Modulated Al_2O_3Grown by Atomic Layer Deposition for InGaZnO Thin-Film Transistors," *ACS Applied Materials & Interfaces* 13, no. 17 (2021): 20349–20360, https://doi.org/10.1021/acsami.1c02597.

14. H.-C. Chen, J.-J. Chen, Y.-F. Tu, et al., "Abnormal Hump Effect Induced by Hydrogen Diffusion During Self-Heating Stress in Top-Gate Amorphous InGaZnO TFTs," *IEEE Transactions on Electron Devices* 67, no. 7 (2020): 2807–2811, https://doi.org/10.1109/TED.2020.2994539.

15. M.-J. Zhao, J.-F. Zhang, J. Huang, et al., "Role of Ambient Hydrogen in HiPIMS-ITO Film During Annealing Process in a Large Temperature Range," *Nanomaterials* 12, no. 12 (2022): 1995, https://doi.org/10.3390/nano12121995.

16. W. Xu, X. Chen, D. Liu, W. Jiang, and B. Yang, "Systematic Thermodynamic and Experimental Studies for Recovering Indium and Tin From Indium Tin Oxide Waste Target With Hydrogen," *Journal of Cleaner Production* 429 (2023): 139328, https://doi.org/10.1016/j.jclepro.2023.139328.

17. D. G. Kim, S. H. Choi, W. B. Lee, et al., "Highly Robust Atomic Layer Deposition-Indium Gallium Zinc Oxide Thin-Film Transistors With Hybrid Gate Insulator Fabricated via Two-Step Atomic Layer Process for High-Density Integrated All-Oxide Vertical Complementary Metal-Oxide-Semiconductor Applications," *Small Structures* 5, no. 2 (2024): 2300375, https://doi.org/10.1002/sstr.202300375.

18. J. Lee, C. H. Choi, T. Kim, et al., "Hydrogen-Doping-Enabled Boosting of the Carrier Mobility and Stability in Amorphous IGZTO Transistors," *ACS Applied Materials & Interfaces* 14, no. 51 (2022): 57016–57027, https://doi.org/10.1021/ACSAMI.2C18094.

19. N. Saito, K. Miura, T. Ueda, T. Tezuka, and K. Ikeda, "High-Mobility and H_2-Anneal Tolerant InGaSiO/InGaZnO/InGaSiO Double Hetero Channel Thin Film Transistor for Si-LSI Compatible Process," *IEEE Journal of the Electron Devices Society* 6 (2018): 500–505, https://doi.org/10.1109/JEDS.2018.2801800.

20. J. E. Medvedeva, K. Sharma, B. Bhattarai, and M. I. Bertoni, "Hydrogen Behavior at Crystalline/Amorphous Interface of Transparent Oxide Semiconductor and its Effects on Carrier Transport and Crystallization," *ACS Applied Materials & Interfaces* 14, no. 34 (2022): 39535–39547, https://doi.org/10.1021/acsami.2c09604.

21. J. A. Spencer, A. L. Mock, A. G. Jacobs, M. Schubert, Y. Zhang, and M. J. Tadjer, "A Review of Band Structure and Material Properties of Transparent Conducting and Semiconducting Oxides: Ga_2O_3, Al_2O_3, In_2O_3, ZnO, SnO_2, CdO, NiO, CuO, and Sc_2O_3," *Applied Physics Reviews* 9, no. 1 (2022): 011315, https://doi.org/10.1063/5.0078037.

22. G. Dingemans, F. Einsele, W. Beyer, M. C. M. van de Sanden, and W. M. M. Kessels, "Influence of Annealing and Al_2O_3 Properties on the Hydrogen-Induced Passivation of the Si/SiO_2 Interface," *Journal of Applied Physics* 111, no. 9 (2012): 093713, https://doi.org/10.1063/1.4709729.

23. Y.-R. Luo, *Comprehensive Handbook of Chemical Bond Energies* (CRC Press, 2007).

24. A. Hussein, B. Kim, K. Verbeken, and T. Depover, "The Effect of Grain Boundary Misorientation on Hydrogen Flux Using a Phase-Field-Based Diffusion and Trapping Model," *Advanced Engineering Materials* 26, no. 22 (2024): 2401561, https://doi.org/10.1002/adem.202401561.

25. H. J. Kim, S. Y. Park, H. Y. Jung, et al., "Role of Incorporated Hydrogen on Performance and Photo-bias Instability of Indium Gallium Zinc Oxide Thin Film Transistors," *Journal of Physics D: Applied Physics* 46, no. 5 (2013): 055104, https://doi.org/10.1088/0022-3727/46/5/055104.

26. Y. Shi, M. Tsuji, H. Cho, S. Ueda, J. Kim, and H. Hosono, "Approach to Low Contact Resistance Formation on Buried Interface in Oxide Thin-Film Transistors: Utilization of Palladium-Mediated Hydrogen Pathway," *ACS Nano* 18, no. 13 (2024): 9736–9745, https://doi.org/10.1021/acsnano.4c02101.

2199160x, 2026, 18, Downloaded from https://advanced.onlinelibrary.wiley.com/doi/10.1002/aelm.70575 by Hanyang University Library, Wiley Online Library on [12/10/2026]. See the Terms and Conditions (https://onlinelibrary.wiley.com/terms-and-conditions) on Wiley Online Library for rules of use; OA articles are governed by the applicable Creative Commons License

27. P. Ágoston, K. Albe, R. M. Nieminen, and M. J. Puska, "Intrinsic n-type Behavior in Transparent Conducting Oxides: A Comparative Hybrid-Functional Study of In_2O_3, SnO_2, and ZnO," *Physical Review Letters* 103, no. 24 (2009): 245501, https://doi.org/10.1103/PhysRevLett.103.245501.

28. J. H. Jeong, S. W. Seo, D. Kim, et al., "Specific Contact Resistivity Reduction in Amorphous IGZO Thin-Film Transistors Through a TiN/IGTO Heterogeneous Interlayer," *Scientific Reports* 14, no. 1 (2024): 10953, https://doi.org/10.1038/s41598-024-61837-2.

29. A. Abliz, "Effects of Hydrogen Plasma Treatment on the Electrical Performances and Reliability of InGaZnO Thin-Film Transistors," *Journal of Alloys and Compounds* 831 (2020): 154694, https://doi.org/10.1016/j.jallcom.2020.154694.

30. A. Kruv, M. J. van Setten, A. Chasin, et al., "In-Poor IGZO: Superior Resilience to Hydrogen in Forming Gas Anneal and PBTI," *ACS Applied Electronic Materials* 7, no. 9 (2025): 4210–4219, https://doi.org/10.1021/acsaelm.5c00383.

31. H. Park, J. Yun, S. Park, et al., "Enhancing the Contact Between a-IGZO and Metal by Hydrogen Plasma Treatment for a High-Speed Varactor (>30 GHz)," *ACS Applied Electronic Materials* 4, no. 4 (2022): 1769–1775, https://doi.org/10.1021/acsaelm.2c00028.

Supporting Information

Additional supporting information can be found online in the Supporting Information section.

Supporting File: aelm70575-sup-0001-SuppMat.doc.

21991606, 2026, 1, Downloaded from https://advanced.onlinelibrary.wiley.com/doi/10.1002/aelm.70575 by Hanyang University Library, Wiley Online Library on [12/10/2026]. See the Terms and Conditions (https://onlinelibrary.wiley.com/terms-and-conditions) on Wiley Online Library for rules of use; OA articles are governed by the applicable Creative Commons License